remote sensing

MDPI

Article

Identification of the Yield of *Camellia oleifera* Based on Color Space by the Optimized Mean Shift Clustering Algorithm Using Terrestrial Laser Scanning

Jie Tang [1,2,3,†], Fugen Jiang [1,2,3,†], Yi Long [1,2,3], Liyong Fu [1,4] and Hua Sun [1,2,3,*]

1 Research Center of Forestry Remote Sensing and Information Engineering, Central South University of Forestry and Technology, Changsha 410004, China; 20191100031@csuft.edu.cn (J.T.); jiangkriging@csuft.edu.cn (F.J.); 20201100036@csuft.edu.cn (Y.L.); fuly@ifrit.ac.cn (L.F.)
2 Key Laboratory of Forestry Remote Sensing Based Big Data and Ecological Security for Hunan Province, Changsha 410004, China
3 Key Laboratory of State Forestry Administration on Forest Resources Management and Monitoring in Southern Area, Changsha 410004, China
4 Research Institute of Forest Resource Information Techniques, Chinese Academy of Forestry, Beijing 100091, China
* Correspondence: sunhua@csuft.edu.cn; Tel.: +86-138-7588-2184
† These authors contributed equally to this work.

Abstract: Oil tea (*Camellia oleifera*) is one of the world's major woody edible oil plants and is vital in providing food and raw materials and ensuring water conservation. The yield of oil tea can directly reflect the growth condition of oil tea forests, and rapid and accurate yield measurement is directly beneficial to efficient oil tea forest management. Light detection and ranging (LiDAR), which can penetrate the canopy to acquire the geometric attributes of targets, has become an effective and popular method of yield identification for agricultural products. However, the common geometric attribute information obtained by LiDAR systems is always limited in terms of the accuracy of yield identification. In this study, to improve yield identification efficiency and accuracy, the red-green-blue (RGB) and luminance-bandwidth-chrominance (i.e., YUV color spaces) were used to identify the point clouds of oil tea fruits. An optimized mean shift clustering algorithm was constructed for oil tea fruit point cloud extraction and product identification. The point cloud data of oil tea trees were obtained using terrestrial laser scanning (TLS), and field measurements were conducted in Changsha County, central China. In addition, the common mean shift, density-based spatial clustering of applications with noise (DBSCAN), and maximum–minimum distance clustering were established for comparison and validation. The results showed that the optimized mean shift clustering algorithm achieved the best identification in both the RGB and YUV color spaces, with detection ratios that were 9.02%, 54.53%, and 3.91% and 7.05%, 62.35%, and 10.78% higher than those of the common mean shift clustering, DBSCAN clustering, and maximum-minimum distance clustering algorithms, respectively. In addition, the improved mean shift clustering algorithm achieved a higher recognition rate in the YUV color space, with an average detection rate of 81.73%, which was 2.4% higher than the average detection rate in the RGB color space. Therefore, this method can perform efficient yield identification of oil tea and provide a new reference for agricultural product management.

Keywords: *Camellia oleifera*; yield identification; terrestrial laser scanning; mean shift; color space

Citation: Tang, J.; Jiang, F.; Long, Y.; Fu, L.; Sun, H. Identification of the Yield of *Camellia oleifera* Based on Color Space by the Optimized Mean Shift Clustering Algorithm Using Terrestrial Laser Scanning. *Remote Sens.* **2022**, *14*, 642. https://doi.org/10.3390/rs14030642

Academic Editor: Krzysztof Stereńczak

Received: 8 December 2021
Accepted: 27 January 2022
Published: 28 January 2022

1. Introduction

Oil tea (*Camellia oleifera*) is one of the world's major woody edible oil plants, and can be used for food, pharmaceuticals, and so on [1–3]. The fruits and processed products of oil tea are raw materials for chemicals, fertilizers, feeds, etc. [4–6]. They can also be used as lubricants and anti-rust oils for industrial applications [7,8]. In addition, oil tea plays a pivotal role in air purification and soil and water conservation. The yield of oil tea is the

main basis for measuring the assets and quality of oil tea forests, which is crucial to the development of the oil tea industry [9,10]. The quantity of oil tea fruits is an important indicator for oil tea products, and can directly measure the yield level. Traditional oil tea yield estimation is mainly performed by manual measurement, which requires considerable time and labor resources and has low efficiency [11–13].

Remote sensing technology can dynamically and quickly obtain rich vegetation information [14,15]. As the main method of data acquisition, images and point clouds have been widely used in agricultural product identification and yield estimation [16–18]. The recognition detection of images requires a large amount of training data, and the recognition detection effect is poor in shady or overexposed conditions, which is not suitable for real-time recognition and detection tasks with high requirements. Light detection and ranging (LiDAR) can penetrate the tree canopy and obtain richer single-wood information. As a representative method, terrestrial laser scanning (TLS), which can provide the spatial geometric and color attributes of the detected targets, is less affected by lighting conditions, has a wide recognition range, and has been widely used in ground target detection, model recovery, and reconstruction [19–23]. Compared with the recognition detection of images, point cloud recognition detection is more intuitive, accurate, and universal. In addition, the target recognition detection achieved by extracting the spatial geometric and color attributes of objects is able to spatially localize the target, which is an effect that cannot be achieved directly by image recognition [24].

Separation and clustering are the main steps of target identification and detection from point cloud data [25]. The main common methods of fruit point cloud separation and recognition include the random sample consensus (RANSAC) algorithm [26,27], Euclidean clustering algorithm [28], region-growing algorithm [29], and color space method [30]. The RANSAC algorithm uses random parameters for estimation and is mostly applied in fitting graphs, lines, and planes. Different thresholds can be set to separate the target elements individually in point cloud separation. The Euclidean clustering algorithm is mainly applied in feature separation, and the point cloud data are separated and extracted according to the similarity of the Euclidean distances of similar feature points. The combination of the region-growing algorithm and principal component analysis has good adaptability and can achieve high-precision extraction of ground feature point cloud data. However, the RANSAC algorithm is mainly suitable for the point cloud separation of building contour elements, and its application effect is limited for complex object structure algorithms. The Euclidean clustering algorithm has a poor effect on the separation of adjacent ground object point clouds, and the region-growing algorithm is only suitable for the separation of regular columns. The red-green-blue (RGB) [31,32] and luminance-bandwidth-chrominance (YUV) [33] color spaces are commonly used; the RGB color space is a linear combination of color attributes, and the YUV color space is obtained by converting RGB attribute values based on the sensitivity of luminance attributes over chrominance attributes. Each region in the color space corresponds to a chromaticity attribute and a saturation attribute, which are used to separate the regions independently of the luminance attribute. This method can also be adapted to situations in which the lighting conditions are constantly changing and can achieve effective recognition of targets in near-color backgrounds [34,35].

Density-based spatial clustering of applications with noise (DBSCAN) clustering [36], maximum-minimum distance clustering [37], the k-means clustering algorithm [38], and mean shift clustering [39–41] are commonly used point cloud clustering methods. DBSCAN clustering is a density-based clustering algorithm that can identify arbitrarily shaped class clusters, but has strict requirements on point cloud density. Maximum–minimum distance clustering is based on the Euclidean distance and works well for spherical object recognition, but the overall recognition accuracy is restricted. The k-means clustering algorithm requires artificially specifying the number of initial cluster centers for class cluster number determination before cluster identification, which limits its application efficiency. Mean shift clustering is an efficient iterative algorithm for nonparametric kernel density gradient

estimation and has been widely used in image smoothing [42], segmentation [43,44], and video tracking [45,46]. However, compared to other algorithms, the accuracy of clustering and recognition is limited in complex situations.

This study aimed to develop an optimized mean shift clustering algorithm to improve the recognition accuracy and detection efficiency of the yield of oil tea fruits. The RGB and YUV color spaces combined with point cloud data extracted by TLS were used to separate the point clouds of oil tea fruits in Changsha County, central China. In addition, to verify the effectiveness of the improved method, the common mean shift clustering, DBSCAN clustering, and maximum–minimum distance clustering methods were established for comparison to provide methodological and technical references for accurate identification and yield estimation of oil tea fruits.

2. Materials and Methods

2.1. Study Area

The study area is one of the largest oil tea bases in Hunan Province, which is located in Changsha County, central China (Figure 1). It has a subtropical monsoon climate with an annual average temperature of 17.6 °C. The annual average frost-free period and annual average sunshine in the study area are 260 days and 1510.9 h, respectively. The soil type is mainly acidic red soil, which is suitable for the growth of oil tea. The oil tea varieties planted are the Xianglin series, which have high yield, disease resistance, and high quality.

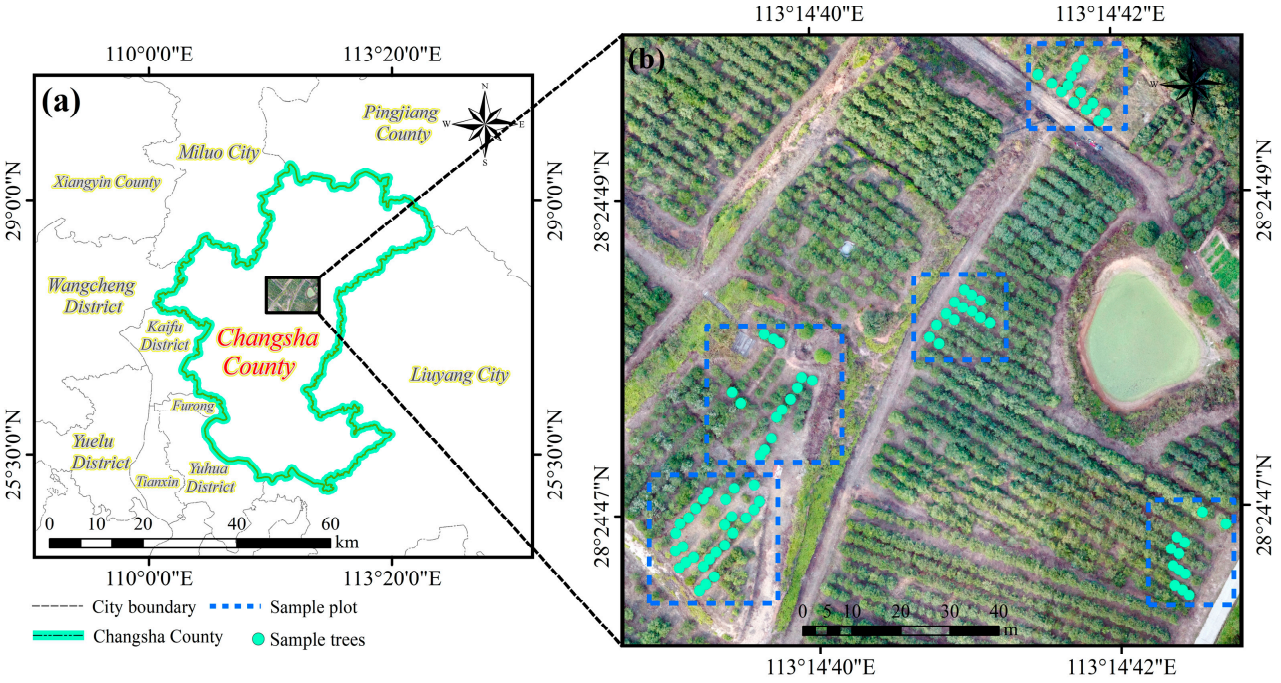

Figure 1. (**a**) Location of the study area and (**b**) the sample tree distribution.

2.2. Framework of This Research

The identification of oil tea yield using terrestrial laser scanning mainly consists of the following four steps: (1) data acquisition and pre-processing; (2) separation of oil tea fruit point cloud data; (3) clustering of oil tea fruit point cloud data; and (4) accuracy evaluation (Figure 2). The study used terrestrial laser scanning to acquire the point cloud data of the tagged oil tea trees, then the point cloud data pre-processing and oil tea fruit yield statistics were performed. The point cloud data of oil tea fruits were separated using RGB and YUV color space according to the difference of color attribute characteristics of oil tea fruits, branches, and leaves, and then the number of class clusters in the point cloud data of separated oil tea fruits was determined by clustering. Finally, the actual number of oil tea fruits was compared and analyzed with the actual number of oil tea fruits.

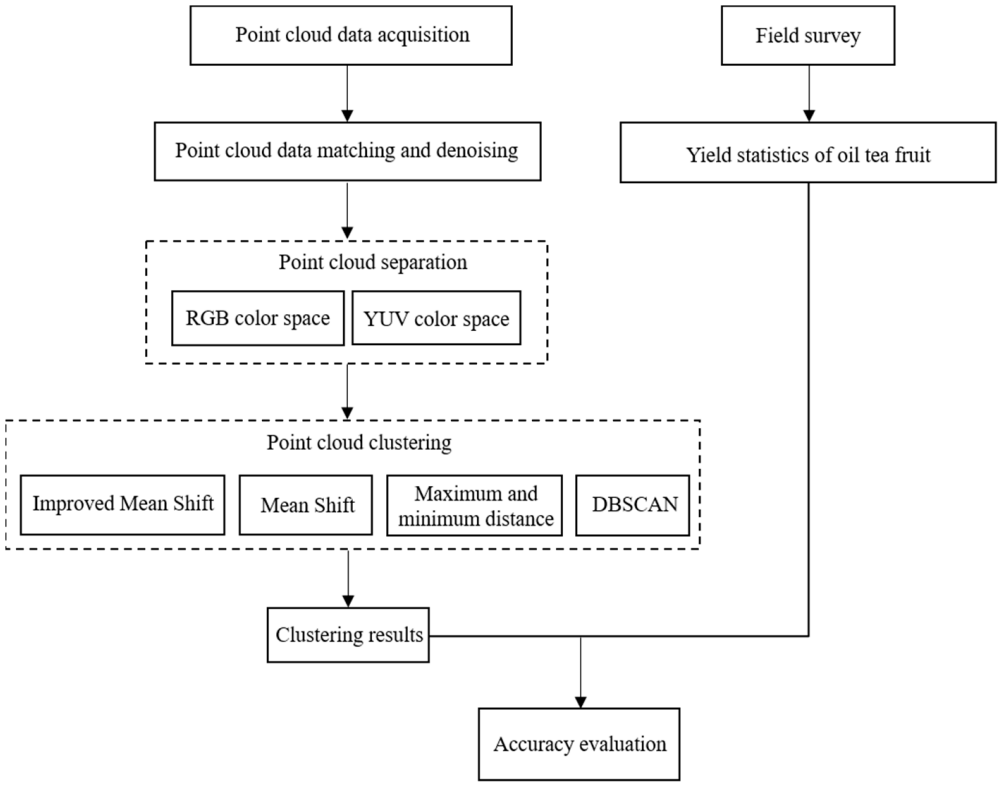

Figure 2. Methodological framework of yield identification of the oil tea fruit in this study.

2.3. Point Cloud Acquisition and Processing

In this study, a Faro Focus 3D X330 terrestrial laser scanning instrument [47,48] was used to acquire the point cloud data of oil tea trees. Since the laser does not penetrate the branches and leaves of oil tea trees, a scanning area containing 2~4 oil tea trees was set as a sample plot to reduce tree shading during the scanning process. Five sample plots in the study area were randomly selected for scanning and point cloud data acquisition (Figure 3). Shrub and weed clearance were performed on the sample plot and its surroundings to improve the quality of the laser point cloud data. The use of multi-station scanning can effectively reduce masking and can compensate for missing data from a single station [49]. To ensure that each oil tea tree in the sample plot could be completely scanned and to reduce the impact of missing point clouds due to mutual shading between oil tea trees, the scanner started at the center of the sample plot, and one scanning station was set at each of the sample plot boundary points in a clockwise direction; each sample plot ultimately included five scanning stations. The standard ball was the basis for matching and stitching the point cloud data scanned from different stations [19,50]. To improve the matching accuracy and efficiency, it was ensured that all the standard balls could not form a straight line, and the height of the standard balls was adjusted by using an automatically retractable measuring rod. The scan resolution and scan quality were set to 1/4 and 4X, respectively. Finally, the obtained scan results contained not only the intensity information of the point cloud, but also the RGB color information of the corresponding object surface.

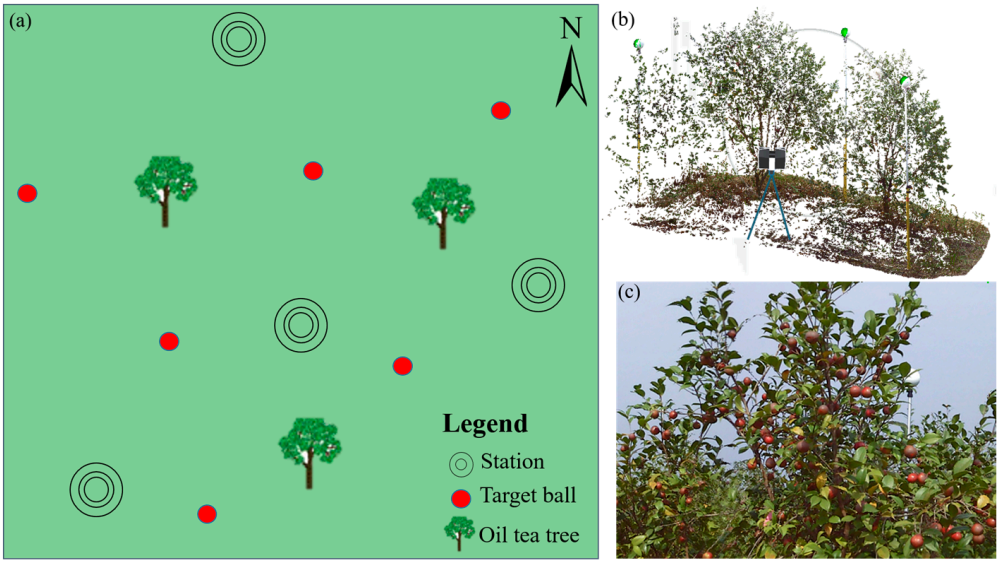

Figure 3. Schematic diagram of the oil tea tree and fruits' point cloud acquisition. (**a**) Scanning stations for point cloud acquisition, (**b**) point cloud data of the oil tea tree and fruits, and (**c**) photograph of the oil tea tree and fruits.

2.4. Measurement of Field Data

To ensure that the samples were representative, five sample plots were randomly selected in the study area for oil tea fruit data collection. The field data were collected in November 2019. The data of 79 oil tea trees were collected, and all the trees were from the Xianglin series. The number of oil tea fruits per tree was counted, and the number of fruits per sample plot was summarized. The statistical information of the final collected oil tea fruits is shown in Table 1.

Table 1. Summary statistics of the fruits in oil tea trees in the study area.

Total Number of Oil Tea Fruits	Mean	Maximum	Minimum	Average Radius of Oil Tea Fruits (cm)
19,066	241	593	38	2.0

2.5. Identification of Oil Tea Fruits Point Clouds

The point cloud data obtained by TLS are dense and high-precision, and they need to be preprocessed with point cloud decomposition and alignment for subsequent identification and separation of the oil tea fruit [51,52]. To improve the accuracy of subsequent point cloud separation, the redundant and noisy data around the oil tea trees were removed using FARO Scene software, and only the point clouds containing the branches, leaves, and fruits of the oil tea trees were retained [53].

Color features are one of the most basic pieces of point cloud data [30,54]. The RGB color space is a combination of red, green, and blue, and is influenced by brightness [31,55]. Through RGB values, the point cloud data of oil tea fruit can be identified, separated, and extracted in the color space. YUV is a nonlinear color space derived from the RGB color space model. YUV describes the color characteristics of the target with luminance attributes and chromatic aberration attributes, and it obtains the attribute values based on the color image attribute values, corrected by color separation magnification [33]. Equation (1) was used to convert the attribute values and obtain the luminance signal Y and the two-color difference signals R-Y and B-Y. Then, the luminance and two-color difference signals were encoded separately, which finally constituted the YUV color space. The luminance and

chromaticity attributes in the YUV color space were separated from each other, and changes in luminance would not influence the color attribute characteristics of the target.

$$\begin{vmatrix} \mathrm{Y} \\ \mathrm{U} \\ \mathrm{V} \end{vmatrix} = \begin{vmatrix} a & b & c \\ d & e & f \\ g & h & j \end{vmatrix} \begin{vmatrix} \mathrm{R} \\ \mathrm{G} \\ \mathrm{B} \end{vmatrix} + \begin{vmatrix} m \\ n \\ k \end{vmatrix} \quad (1)$$

where a, b, c, d, e, f, g, h, and j are conversion factors, which are defined by the standard of the International Telecommunication Union Radiocommunication Sector Broadcasting Service (Television) (ITU-R-BT) [56], and m, n, and k are constants that can limit the range of each YUV attribute value to [0, 255].

The scanning result of TLS can yield not only the intensity information of the point cloud, but also the RGB color information of the object surface [57]. After extracting the RGB values in the point cloud data of the oil tea tree, the luminance Y and the color difference attribute values U and V can be obtained by Equation (1); finally, the point cloud data of the oil tea fruits can be separated according to the YUV attribute values of the oil tea fruits.

2.6. Clustering Method for Oil Tea Fruits

The mean shift clustering algorithm is a statistical iterative algorithm in which the iterative process first calculates the offset mean of the current point, moves the point to that offset mean, uses it as a new starting point, and continues to move it until the final condition is met [58]. However, its low accuracy and long processing iteration time limit its application [41]. In this study, to improve the recognition accuracy of oil tea fruits, the number of oil tea fruit clusters in the point cloud data was obtained by clustering, and the goal was to find the center of mass of the oil tea fruit clusters to cluster the point cloud data. To reduce the impact of incomplete TLS scanning and to improve the efficiency of the algorithm operation, the Euclidean distance between individual cluster centers was calculated to determine whether more than one cluster belonged to the same oil tea fruit after the centers of the clusters were determined. The main steps for improving the mean shift clustering algorithm are as follows:

An arbitrary point from the unlabeled point cloud data was selected as the cluster center, and a range was extracted according to the set cluster radius, which can be regarded as a high-dimensional sphere internal region− with a center and radius and is defined by Equation (2).

$$\mathrm{Q}_{radius}(x) = \sqrt{(y|(y-x)(y-x)^{\mathrm{T}})} \leq radius \quad (2)$$

where $\mathrm{Q}_{radius}(x)$ is the set of y points; x is the spherical coordinate matrix; and y is the coordinate matrix of a single point in the point cloud. *radius* was set to 2 cm, as determined by the radius of the oil tea fruit measured in the study area.

Equation (3) is used to calculate the Euclidean distance between the remaining points and the selected point, retrieve the points in the region with the center as the sphere and the radius of the sphere as the radius, classify the eligible data points into class cluster C, and record the data points in this class cluster to increase the number of visits by 1.

$$\mathrm{dist}(a,b) = \sqrt{(x_a - x_b)^2 + (y_a - y_b)^2 + (z_a - z_b)^2} \quad (3)$$

where (x_a, y_a, z_a) is the 3D spatial coordinate of point a and (x_b, y_b, z_b) is the coordinate of point b.

The mean of all data points in class cluster *C* is considered the new cluster center.

$$\begin{cases} \overline{X} = \frac{1}{k} \sum_{x_k \epsilon Q radius(Ck)} x_k \\ \overline{Y} = \frac{1}{k} \sum_{y_k \epsilon Q radius(Ck)} y_k \\ \overline{Z} = \frac{1}{k} \sum_{z_k \epsilon Q radius(Ck)} z_k \end{cases} \quad (4)$$

where k is the number of points of the set Q_{radius} (Ck) in the class cluster Ck, and (x_k, y_k, z_k) is the 3D spatial coordinate of the kth point.

The Euclidean distances between the new cluster center and the remaining cluster center, the current cluster center Ck, and other existing cluster centers C were calculated. If the distance is less than or equal to the convergence threshold (i.e., the average radius of oil tea fruit), the class clusters Ck and C are merged, and the frequency counts of the data point occurrences are merged correspondingly. Otherwise, C is treated as a new class cluster. The above steps are repeated until all points are marked. Based on the number of visits to each class cluster, the data points are grouped into the most visited class clusters until all points belong to class clusters.

In addition, to verify the effectiveness of this improved method, the common mean shift clustering algorithm, the DBSCAN clustering algorithm, and the maximum–minimum distance clustering algorithm were established for comparison.

The threshold radius r in DBSCAN indicates the range of the neighborhood centered at point P (Equation (5)). P_{Min} is the minimum number of points in the neighborhood of point P with a radius of r. The distances between point P and the remaining points were calculated, where p is the coordinate matrix of P and p_i is the coordinate matrix of the ith point, and then the number of points within the radius r of point P was counted (Equation (6)). In Equation (7), $N_r(P)$ includes all points with a distance of no more than r from point P. If the number of points included in $N_r(P)$ is not less than P_{Min}, then P is set as the core point, and then the sample set that can reach the density of all core objects is identified as a cluster.

$$\mathrm{Dist}(P, p_i) = \sqrt{(p - p_i)(p - p_i)^T} \quad (5)$$

$$N_r(P) = \{\mathrm{Dist}(P, p_i) \leq r\} \quad (6)$$

$$|N_r(P)| \geq P_{Min} \quad (7)$$

For the maximum–minimum distance clustering algorithm, the first cluster center X_1 is randomly selected in the sample point cloud data, and the second cluster center X_2 is defined as the point farthest from X_1. The d_N is the set consisting of the distances from each cluster center to all sample points in the algorithm (Equation (8)), where d_{Nn} is the distance from the Nth cluster center X_N to the nth sample point. Equation (9) is used to determine whether there is a next cluster center, where $\mathrm{Min}(d_N)$ is a distance subset of d_N with the smallest sum of elements in that distance subset, m is the test parameter, $|X_N - X_{N-1}|$ is the distance from X_N to X_{N-1}, and $\mathrm{Max}\{\mathrm{Min}(d_N)\}$ is the maximum value in the set of $\mathrm{Min}(d_N)$. If Equation (9) holds, then the sample point corresponding to $\mathrm{Max}\{\mathrm{Min}(d_N)\}$ is the (N + 1)th cluster center, otherwise it is considered that there is no new cluster center. After determining all the cluster centers, the distances between each point and the cluster center are calculated, and the points are grouped into the class cluster corresponding to the nearest cluster center (Equation (10)), where Yj is the jth point in the point cloud dataset D, X_i is the ith cluster center, and yj and xi are the coordinate matrices of Y_j and X_i, respectively.

$$d_N = \{(d_{11}, d_{21}, d_{31} \ldots\ldots d_{N1}), (d_{11}, d_{22}, d_{32} \ldots\ldots d_{N2}) \ldots\ldots, (d_{1n}, d_{2n}, d_{3n} \ldots\ldots d_{Nn})\} \quad (8)$$

$$\mathrm{Max}\{\mathrm{Min}(d_N)\} > m * |X_N - X_{N-1}| \quad (9)$$

$$X_i(Y_j) = \{Y_j \in D|\text{Min}(\text{dist} = \sqrt{(y_j - x_i)(y_j - x_i)^T})\} \quad (10)$$

2.7. Algorithm Accuracy Assessment

The average completion rate ($\overline{P}$) and the variance of the detection ratio (D) are used to evaluate the recognition effectiveness and stability of the four clustering algorithms [59,60]. The detection rate, also called the recall rate, represents the ratio of the number of targets detected by recognition to the total number of targets in the sample. The average completion rate is the average of the completion rates of all samples and is calculated as in Equation (11). The variance of the detection ratio is the average of the squared deviation of the detection ratio of each strain from the average detection ratio, which is calculated as in Equation (12).

$$\overline{P} = \frac{1}{N}\sum_{i=1}^{N}\frac{TP_i}{NP_i} \quad (11)$$

$$D = \frac{1}{N-1}\sum_{i=1}^{N}(P_i - \overline{P})^2 \quad (12)$$

where $\overline{P}$ is the average detection rate, which is the average detection ratio of oil tea fruits in this study; N is the number of oil tea plants; TP_i is the number of oil tea fruits detected; NP_i is the total number of oil tea fruits of a single plant; and P_i is the detection rate of oil tea fruits on a single oil tea tree. The larger $\overline{P}$ is, the better the clustering recognition effect of the clustering algorithm. The smaller D is, the higher the stability of the clustering algorithm.

3. Results

3.1. Point Cloud Separation Results

The key to point cloud separation is to determine the threshold value of the color attributes of branches and fruits; the colors of leaves and fruits are distinctly different, and the RGB attribute values differ greatly and can be separated by determining the relative sizes of the red and green attribute values. The results of the color feature attributes of the point cloud of ripe oil tea fruit in the RGB color space and YUV color space are shown in Table 2. To eliminate the point cloud data other than that of ripe oil tea fruit to a greater extent, the color attribute values of the color space where all point cloud data are located were subtracted from the corresponding lower threshold values when the RGB color space and YUV color space were separated.

An attribute value less than 0 after subtraction means that the color feature attribute value of the point does not satisfy the threshold distribution condition of ripe oil tea fruit in the corresponding color space; the data are then filtered and extracted according to the size relationship between the color features R and G and U and V of ripe oil tea fruit. The effect of multiple identifications and missed detections in clustering can be reduced by improving the Euclidean distance determination step in the mean shift clustering algorithm.

Table 2. Summary statistics of the trees and fruits of the oil tea in the study area.

Color Space	Attribute Characteristics	Maximum Value	Minimum Value
RGB	R	255	200
	G		250
	B		250
YUV	Y		160
	U		220
	V		220

The randomly selected oil tea tree No. 02 was used as an example for point cloud separation visualization (Figure 4). The numbers of points in the point cloud data of single oil tea fruits extracted by separating the RGB color space and YUV color space were 1485 and 8839, respectively, which indicated that the point cloud data separated by the YUV color space had higher density and could be extracted more completely for oil tea fruit.

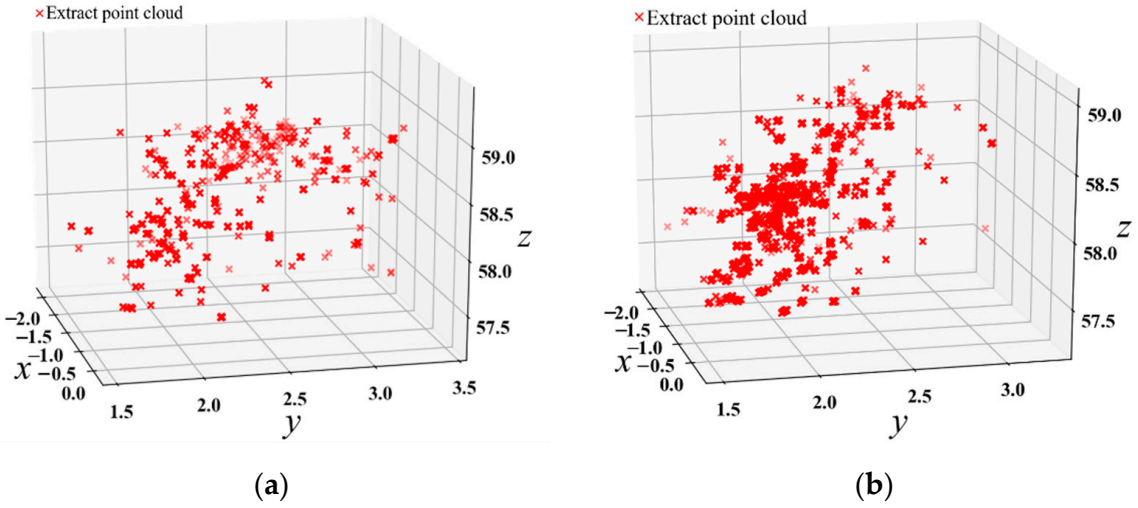

Figure 4. Separation result for oil tea fruit in (**a**) the RGB color space and (**b**) the YUV color space.

The maximum, minimum, and average values of the color characteristics of the point cloud data separated in the RGB color space and YUV color space were calculated separately for comparison (Figure 5). In the RGB color space, the maximum values of the three attributes were similar, while the average values decreased, and the minimum values of G and B were similar. In the YUV color space, the values of the maximum, average, and minimum values of the three attributes were (255, 118, 181), (160, 64, 121), and (175, 88, 138), whose differences were more obvious than the RGB color space. The maximum values of Y, R, G, and B were similar, and the average values from high to low were R, G, Y, and B; however, the average values of U and V were lower than those of R, G, and B.

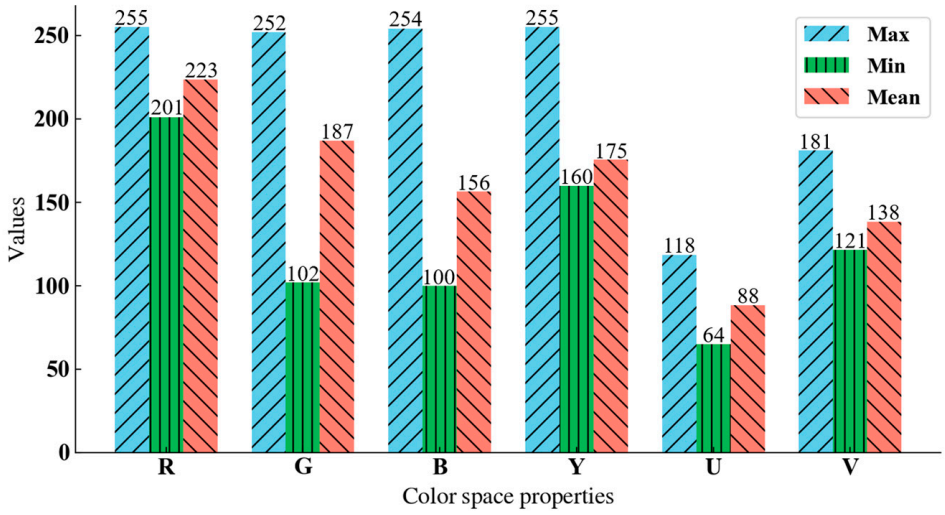

Figure 5. Comparison of the RGB and YUV attributes extracted from the point clouds of oil tea fruit.

3.2. Clustering Analysis

The improved mean shift clustering method and three common clustering algorithms (mean shift clustering, DBSCAN clustering, and maximum–minimum distance clustering) were used to identify the number of clusters of oil tea fruit based on the point cloud data separated by the RGB color space and YUV color space, and the results are shown in Table 3. In the RGB color space, the average detection ratio of improved mean shift clustering was 79.33%, which was 9.04% higher than that of traditional mean shift clustering, and the smaller variance indicates that improved mean shift clustering was more stable than the other clustering methods. In the YUV color space, the average detection rate of improved mean shift clustering was 81.73%, which was 7.05% higher than that of traditional mean shift clustering. The average detection rate of the improved mean shift clustering algorithm increased by 2.4% in the YUV color space compared to the RGB color space. The improved mean shift clustering algorithm had the best recognition effect in both color spaces. However, the DBSCAN clustering algorithm had the worst clustering results in both the RGB color space and YUV color space.

Table 3. Comparison of the results for the clustering methods in the RGB and YUV color spaces.

Color Space	Clustering Method	Highest Detection Rate/%	Minimum Detection Rate/%	$\overline{P}$	Number of Detected Fruits	D
RGB	Improved Mean Shift	96.56	20.27	79.33	14,929	0.0127
	Mean Shift	89.19	17.37	70.29	13,039	0.0150
	DBSCAN	51.47	6.24	24.80	3855	0.0124
	Maximum–Minimum Distance	98.48	19.31	75.42	13,992	0.0173
YUV	Improved Mean Shift	98.13	30.22	81.73	15,210	0.0134
	Mean Shift	93.46	26.79	74.68	13,786	0.0127
	DBSCAN	67.39	1.32	19.38	2665	0.0178
	Maximum–Minimum Distance	93.18	26.48	70.95	12,893	0.0151

The RGB color space clustering results were visualized and mapped, and the distribution of the class clusters identified by the common mean shift clustering algorithm, improved mean shift clustering algorithm, and maximum–minimum distance clustering algorithm were roughly similar, while the locations of the clusters of oil tea fruit identified by the DBSCAN clustering algorithm shifted significantly. Figures 6 and 7 show the number and ratio distribution, respectively, of fruits detected by the four clustering algorithms for the 79 oil tea trees in the study area. The improved mean shift clustering algorithm performed the best recognition, followed by the maximum–minimum distance clustering algorithm. However, the DBSCAN clustering algorithm had the worst clustering recognition effect. RGB is more sensitive to light conditions, which means that the separated partial strain of the oil tea fruit point cloud is of poor quality, resulting in the improved mean shift clustering algorithm in the RGB color space having similar clustering detection ratios for partial oil tea fruit point cloud data to those of other algorithms.

In the YUV color space (Figure 8), the improved mean shift clustering algorithm was still the best, with an average detection ratio of 81.73%. In the YUV color space, the average detection ratio of traditional mean shift clustering improved by 3.73% compared to the maximum–minimum distance clustering algorithm. As the density of the point cloud data of oil tea fruits separated in the YUV color space increased, the quality of the recognition effect of the DBSCAN clustering algorithm decreased further, and the average detection ratio changed from 24.80% to 19.38% (Figure 9).

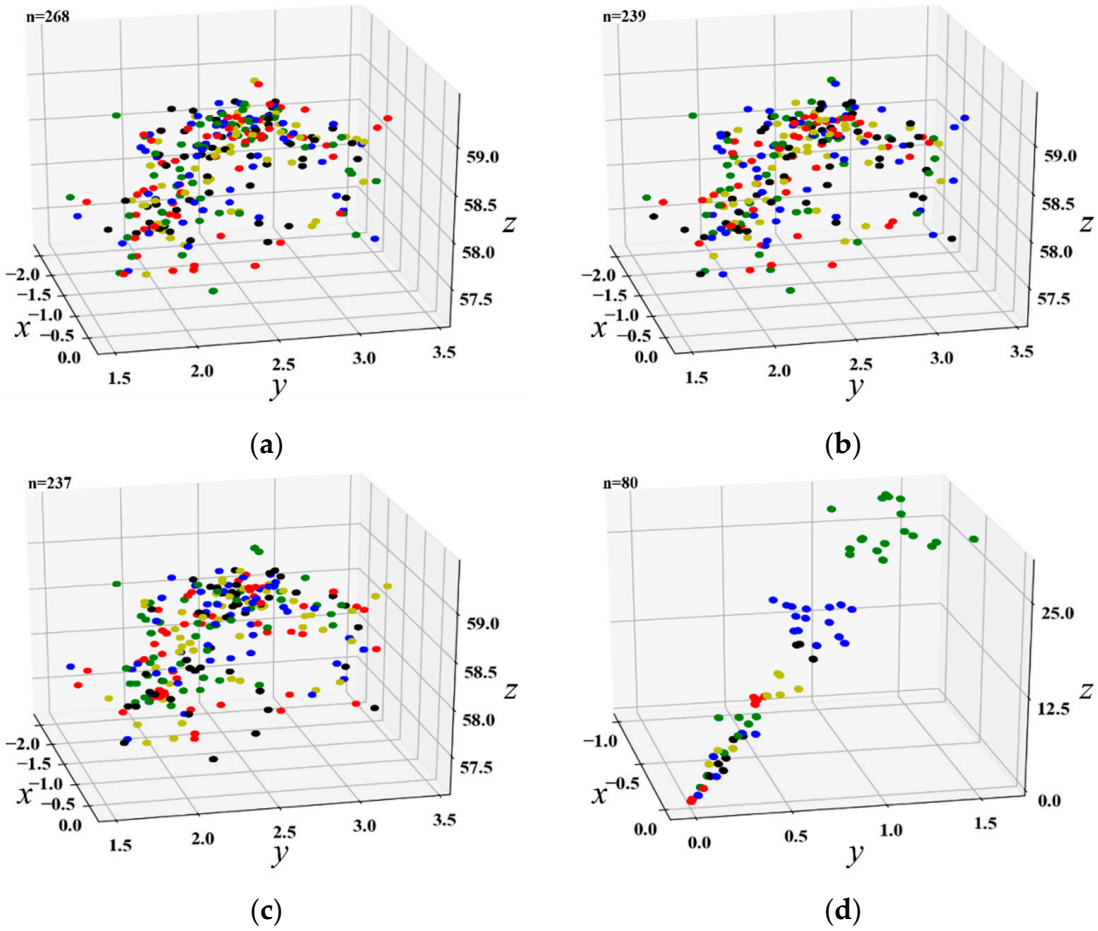

Figure 6. The fruit number results based on the RGB color space clustered by the (**a**) improved mean shift, (**b**) common mean shift, (**c**) maximum–minimum distance, and (**d**) DBSCAN clustering methods.

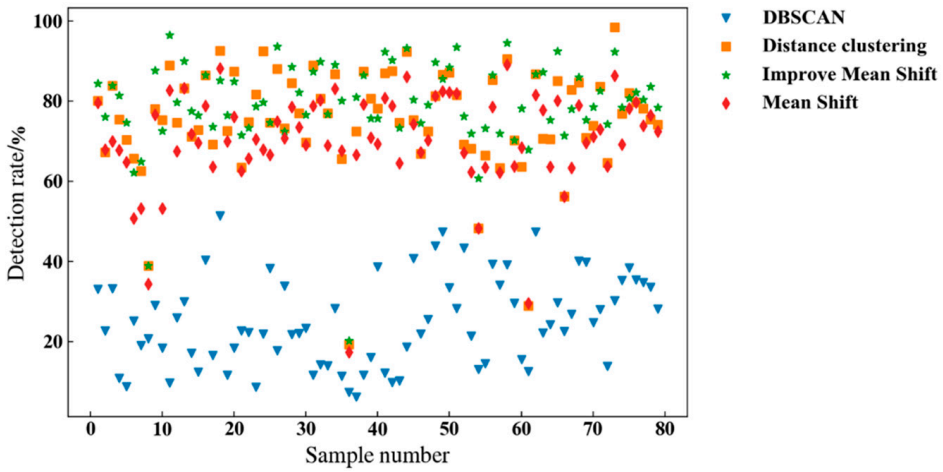

Figure 7. Detection ratio of oil tea fruit based on the RGB color space.

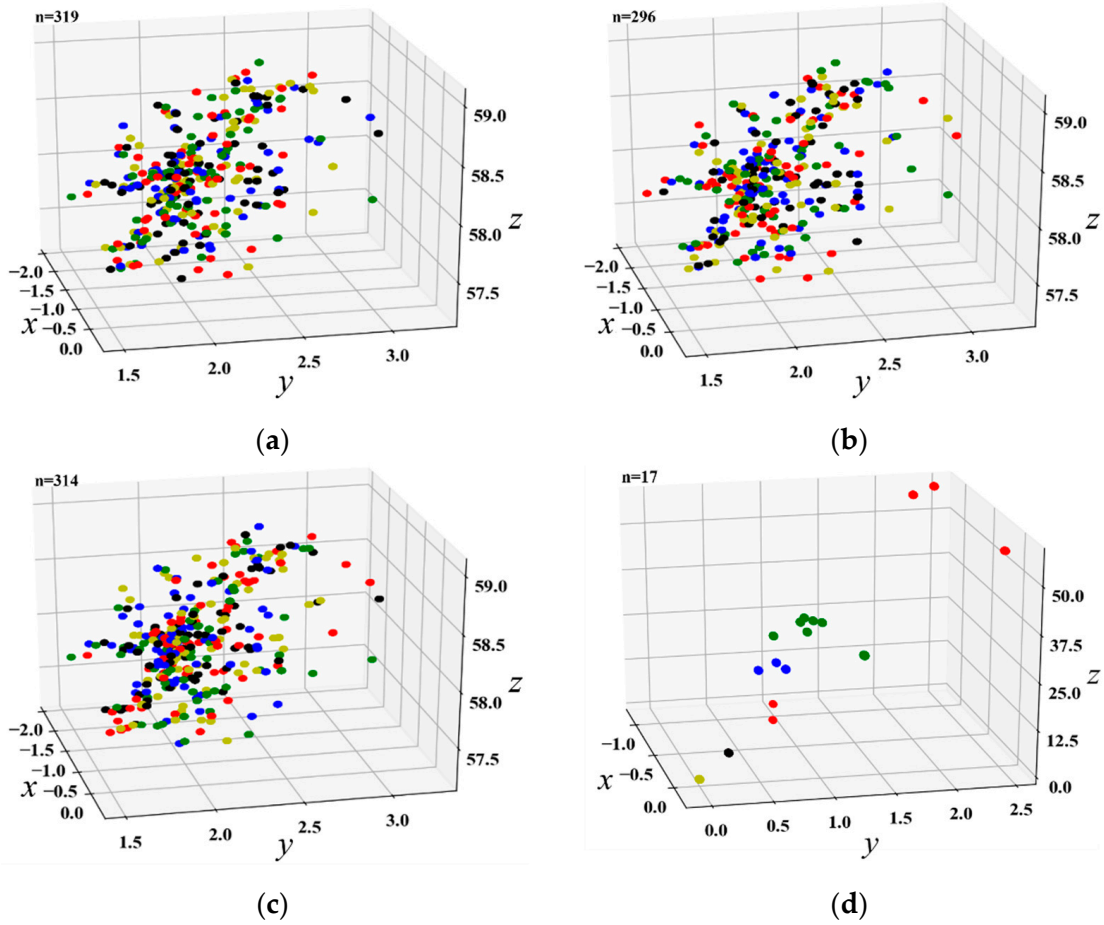

Figure 8. The fruit number results based on the YUV color space clustered by the (**a**) improved mean shift, (**b**) common mean shift, (**c**) maximum–minimum distance, and (**d**) DBSCAN clustering methods.

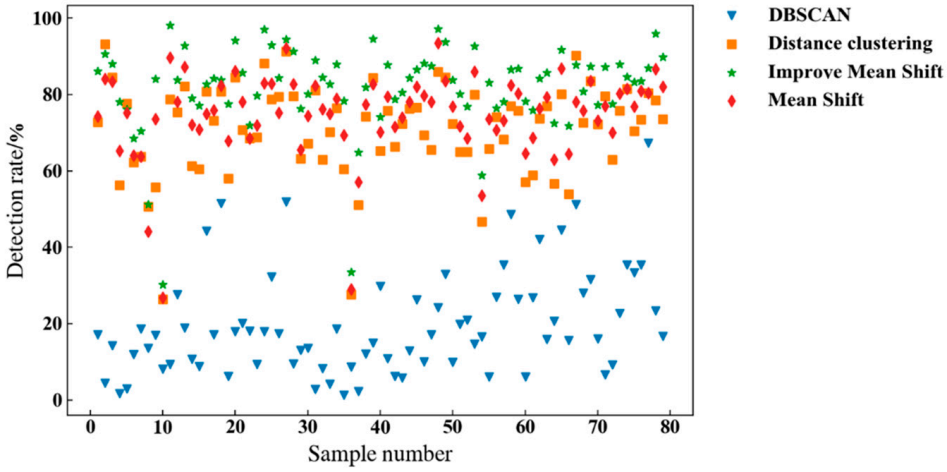

Figure 9. Detection ratio of oil tea fruit based on the YUV color space.

4. Discussion

4.1. Point Cloud Acquisition

Airborne LiDAR enables yield acquisition of agricultural products due to its convenience and high efficiency [61]. However, the quality of the acquired point clouds is limited in complex terrain and forest conditions [62]. TLS with high spatial resolution can acquire

high-quality 3D point cloud data of the target in a detailed and accurate manner, which provides a new direction for yield estimation of agricultural products and has the potential to efficiently and automatically acquire the yield and quantity of agricultural products [63].

The point cloud density, an important attribute of data quality, was negatively correlated with the distance between the scanned sites and the oil tea trees, and this could significantly affect the detection ratio of oil tea fruits. The density of point cloud data separated in the YUV space increased by 51.94% compared with the density in the RGB space and provided a more accurate description of the morphological characteristics of oil tea fruits. In addition, the improved mean shift algorithm, which obtained the best results, increased the average detection rate of oil tea fruits in the YUV color space by 2.4% (Table 3).

The parameter settings of the terrestrial laser scanner can also significantly affect the quality of point cloud data acquisition [64]. The resolution characterizes the highest resolution capability of the instrument for the target and represents the smallest feature parameter for which the terrestrial laser scanner can recognize the study target [65]. The resolution parameter directly determines the density of the point cloud, which has an important impact on the subsequent cluster identification. The point cloud data require sufficient resolution to extract the geometry of the study target and thus enable recognition detection [66]. The resolution parameter of the terrestrial laser scanner can be set low to obtain high scanning efficiency, but the measurement point spacing will be large, resulting in a sparse point cloud density, making it difficult to describe the fine features of the scanned target; when the resolution is too high, the measurement point spacing is small and can accurately reflect the details of the object, but the scanning efficiency is low. To balance the point cloud quality and acquisition efficiency, different resolutions were set in each sample plot for testing and comparison. A resolution of 1/2 yielded a confidence of 96.39% that the target details could be identified, but the scanning time was too long. A resolution of 1/8 yielded lower confidence and fewer acquisition points. A resolution of 1/4 achieved 7% higher confidence than 1/8, and the scanning time was moderate, which can enable high point cloud quality and high scanning efficiency at the same time. Finally, five scanning stations were set up within each sample plot in our study to ensure the quality of the collected point clouds. The size of the scanned sample area is also an important factor in the quality and efficiency of TLS. The point cloud density decreases as the scanning distance increases. In this study, to obtain complete fruit point cloud data, the area covered by 2~4 oil tea trees was used as the scanning range, and scanning stations were set up at different angles; the final point cloud quality and scanning efficiency achieved the efficient identification of fruits.

4.2. Clustering Algorithm for Oil Tea Fruit Identification

The clustering algorithm can significantly affect the recognition of oil tea yield [67]. For the RGB and YUV color spaces, the average detection ratios of the improved mean shift clustering algorithm were 79.33% and 81.73%, respectively, which were 9.04% and 7.05% higher, respectively, than those of the traditional mean shift clustering algorithm and could effectively estimate oil tea fruit yield.

Figure 10 shows the detection results of the four clustering algorithms. With the increase in point cloud density, the number of oleaginous fruits detected by the improved mean shift clustering algorithm and the traditional mean shift clustering algorithm increased, while the number of oleaginous fruits detected by the DBSCAN clustering algorithm and the maximum–minimum distance clustering algorithm decreased. The improved mean shift clustering algorithm takes both distance and density into account.

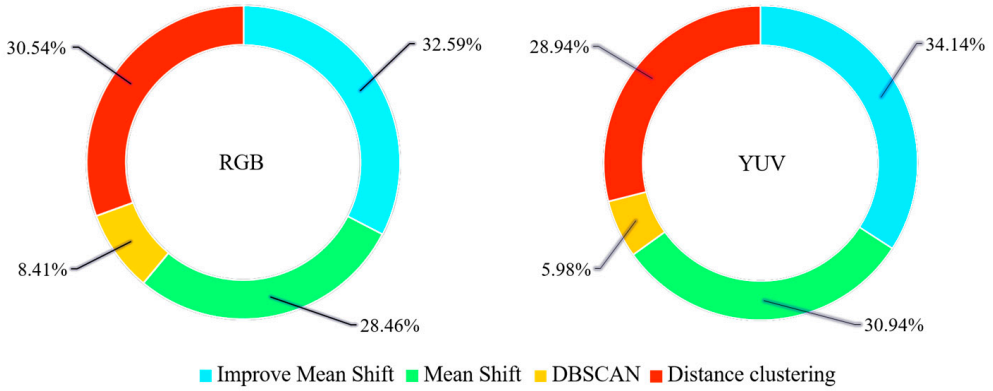

Figure 10. Detection results of the four clustering algorithms in the RGB and YUV color spaces.

DBSCAN is more sensitive to the point cloud density and clustering spacing difference, and the point cloud density separated by the YUV color space is higher, but the existence of clumping in oil tea fruits limits its application [36]. An increase in point cloud density will cause the selection of the initial clustering centers to be too dense and the phenomenon of clustering conflict to arise, which will reduce the effect of the maximum–minimum distance clustering algorithm [37].

4.3. Uncertainty, Limitations, and Prospects

There are several factors that can cause uncertainty in the process of oil tea yield identification using point cloud data, mainly including device operation error and errors caused by the data acquisition environment and target attributes [68].

The main TLS instrument errors are laser sensor errors, equipment operation errors, and laser point cloud data stitching errors [69]. A laser sensor error is an error in the collected data caused by the atmospheric refraction of the laser pulse signal during the transmitting and receiving process [70]. In this study, to minimize the influence of atmospheric refraction, point cloud acquisition was avoided in weather with strong direct light.

A device operation error is an error caused by self-shaking or the deviation of the scanning center position due to bearing plane movement during point cloud data acquisition [69]. To minimize the equipment operation error, the center position of the scanner should be kept stationary during the operation of the 3D laser scanner. FARO Focus 3D X330 laser scanner single-station scanning point cloud data stitching processing was carried out in SCENE software [53], which is a fully automated process, and there is no human operation factor interference caused by point cloud data stitching errors. When the research object is shaken due to high winds, the reflection position of the laser pulse signal will be shifted, causing errors [70]. In this study, the size of the canopy of the fruit trees has different effects on point cloud data acquisition. Too large a canopy will strengthen the shading effect between the fruit trees and the degree of leaf coverage, resulting in incomplete scanning of the instrument and partial loss of the point cloud data [71]. To reduce the influence of the differences between canopy structures, a sample scan plot was set up with a small number of oil tea plants, and multiple scan stations were set up at the same time to collect oil tea point cloud data from different angles.

Optical remote sensing images have certain advantages in extracting large-scale vegetation parameters, but their penetration is poor [72]; LiDAR can obtain high-precision three-dimensional spatial structure information but lacks spectral information. It is very difficult to rely on LiDAR point cloud data alone for the classification and identification detection of research targets [73]. LiDAR data and traditional remote sensing data can be combined to complement each other with different data sources and take advantage of multisource remote sensing data [74], which will help in performing the acquisition and identification detection of research target information. Combined operations on different

data can compensate for the limitations of single data to a certain extent and can enable the use of more feature information (e.g., spectral information, structural information, and texture features) to improve the accuracy of research target identification detection [74].

Although ground-based LiDAR can acquire high-precision and high-density 3D structure information on fruit trees, its scanning range is limited [63]. Airborne LiDAR can acquire a large range of fruit tree structure parameters, but its point cloud density is low. In terms of the observation range and the completeness and fineness of the extracted parameters, the two systems have good complementarity, but the real fusion of airborne and ground-based point clouds is still difficult to achieve due to the large difference in point cloud density between the two types of data and the mismatch of observation ranges [74].

LiDAR provides a new perspective for yield estimation of agricultural products from the perspective of three-dimensional space and further deepens the knowledge of yield estimation systems [61]. How to make full use of the data advantages of LiDAR technology itself to achieve accurate yield estimation has gradually become a research hotspot in LiDAR application fields [75]. In addition, the traditional point cloud recognition detection method depends greatly on the feature parameters of the research target, and the accuracy of point cloud recognition detection is poor for more complex scenes [76]. Methods such as deep learning algorithms can extract the features of the point cloud data of the research target well and can convert 3D point clouds into 2D images of multiple viewpoints for recognition detection, which has the potential to enable fast crop yield recognition [77–79].

5. Conclusions

This study obtained the point cloud data of oil tea trees through TLS, separated the point clouds of oil tea fruits based on the RGB and YUV color spaces, and then constructed an improved mean shift clustering algorithm for oil tea fruit clustering and identification. The traditional mean shift clustering algorithm, DBSCAN clustering algorithm, and maximum–minimum distance clustering algorithm were also used for comparison and analysis. The results show that the improved mean shift algorithm significantly improved the clustering effect on the point cloud data of oil tea compared to that of the traditional algorithm. Compared with the RGB color space, the YUV color space had a better recognition separation effect, and the separated point clouds had a higher density and can yield more complete point cloud data. TLS point cloud data combined with color space can be used to estimate the yield of oil tea fruit to improve the efficiency of large-scale identification of Camellia oleifera fruit. The improved method has robust stability and repeatability, and can provide a new reference for other yield estimation.

Author Contributions: Conceptualization and methodology, H.S., L.F. and J.T.; Validation, F.J. and Y.L.; Formal analysis, J.T.; Investigation, F.J., J.T. and H.S.; Draft, F.J., H.S. and J.T.; Supervision, H.S. and L.F.; Review, editing, and revision, Y.L. and J.T.; Funding acquisition, H.S. All authors have read and agreed to the published version of the manuscript.

Funding: This research was funded by the Scientific Research Fund of Hunan Provincial Forestry Department, grant number XLK201986; the project of the National Natural Science Foundation of China, grant number 31971578; and the Scientific Research Fund of Changsha Science and Technology Bureau, grant number kq2004095.

Institutional Review Board Statement: Not applicable.

Informed Consent Statement: Not applicable.

Data Availability Statement: Not applicable.

Conflicts of Interest: The authors declare no conflict of interest.

References

1. Zhang, S.; Li, X. Hypoglycemic activity in vitro of polysaccharides from Camellia oleifera Abel. seed cake. *Int. J. Biol. Macromol.* **2018**, *115*, 811–819. [CrossRef] [PubMed]
2. Yeh, W.; Ko, J.; Huang, W.; Cheng, W.; Yang, H. Crude extract of Camellia oleifera pomace ameliorates the progression of nonalcoholic fatty liver disease via decreasing fat accumulation, insulin resistance and inflammation. *Br. J. Nutr.* **2019**, *123*, 508–515. [CrossRef] [PubMed]
3. Lili, L.; Cheng, X.; Teng, L.; Wang, Y.; Dong, X.; Chen, L.; Zhang, D.; Peng, W. Systematic Characterization of Volatile Organic Components and Pyrolyzates from Camellia oleifera Seed Cake for Developing High Value-added Products. *Arab. J. Chem.* **2017**, *11*, 802–814. [CrossRef]
4. Chen, Y.; Yang, C.; Chang, M.; Ciou, Y.; Huang, Y. Foam Properties and Detergent Abilities of the Saponins from Camellia oleifera. *Int. J. Mol. Sci.* **2010**, *11*, 4417–4425. [CrossRef] [PubMed]
5. Ye, Y.; Guo, Y.; Luo, Y. Anti-Inflammatory and Analgesic Activities of a Novel Biflavonoid from Shells of Camellia oleifera. *Int. J. Mol. Sci.* **2012**, *13*, 12401–12411. [CrossRef]
6. Zhu, J.; Zhu, Y.; Jiang, F.; Xu, Y.; Ouyang, J.; Yu, S. An integrated process to produce ethanol, vanillin, and xylooligosaccharides from Camellia oleifera shell. *Carbohydr. Res.* **2013**, *382*, 52–57. [CrossRef]
7. Ma, B.; Huang, Y.; Nie, Z.; Qiu, X.; Su, D.; Wang, G.; Yuan, J.; Xie, X.; Wu, Z. Facile synthesis of Camellia oleifera shell-derived hard carbon as an anode material for lithium-ion batteries. *RSC Adv.* **2019**, *9*, 20424–20431. [CrossRef]
8. Xu, T.; Cui, K.; Chen, J.; Wang, R.; Wang, X.; Chen, L.; Zhang, Z.; He, Z.; Liu, C.; Tang, W.; et al. Biodiversity of Culturable Endophytic Actinobacteria Isolated from High Yield Camellia oleifera and Their Plant Growth Promotion Potential. *Agriculture* **2021**, *11*, 1150. [CrossRef]
9. Tu, J.; Chen, J.; Zhou, J.; Ai, W.; Chen, L. Plantation quality assessment of Camellia oleifera in mid-subtropical China. *Soil Tillage Res.* **2019**, *186*, 249–258. [CrossRef]
10. Ye, H.-L.; Chen, Z.-G.; Jia, T.-T.; Su, Q.-W.; Su, S.-C. Response of different organic mulch treatments on yield and quality of Camellia oleifera. *Agric. Water Manag.* **2020**, *245*, 106654. [CrossRef]
11. Murat, O.; Bulent, T.; Tuncay, D.; Erkan, B. An Effective Yield Estimation System Based on Blockchain Technology. *IEEE Trans. Eng. Manag.* **2020**, *67*, 1157–1168. [CrossRef]
12. Wulfsohn, D.; Zamora, F.A.; Téllez, C.P.; Lagos, I.Z.; García-Fiñana, M. Multilevel systematic sampling to estimate total fruit number for yield forecasts. *Precis. Agric.* **2012**, *13*, 256–275. [CrossRef]
13. Michael, M.; Kevin, T.; Jesslyn, B. Optimizing a remote sensing production efficiency model for macro-scale GPP and yield estimation in agroecosystems. *Remote Sens. Environ.* **2018**, *217*, 258–271. [CrossRef]
14. Liu, Y.; Wang, J.; Dong, J.; Wang, S.; Ye, H. Variations of Vegetation Phenology Extracted from Remote Sensing Data over the Tibetan Plateau Hinterland during 2000–2014. *J. Meteorol. Res.* **2020**, *34*, 786–797. [CrossRef]
15. Tian, F.; Brandt, M.; Liu, Y.Y.; Verger, A.; Tagesson, T.; Diouf, A.A.; Rasmussen, K.; Mbow, C.; Wang, Y.; Fensholt, R. Remote sensing of vegetation dynamics in drylands: Evaluating vegetation optical depth (VOD) using AVHRR NDVI and in situ green biomass data over West African Sahel. *Remote Sens. Environ.* **2016**, *177*, 265–276. [CrossRef]
16. Sun, S.; Li, C.; Chee, P.W.; Paterson, A.H.; Jiang, Y.; Xu, R.; Robertson, J.S.; Adhikari, J.; Shehzad, T. Three-dimensional photogrammetric mapping of cotton bolls in situ based on point cloud segmentation and clustering. *ISPRS J. Photogramm. Remote Sens.* **2020**, *160*, 195–207. [CrossRef]
17. Horng, G.-J.; Liu, M.-X.; Chen, C.-C. The Smart Image Recognition Mechanism for Crop Harvesting System in Intelligent Agriculture. *IEEE Sens. J.* **2019**, *20*, 2766–2781. [CrossRef]
18. Xing, S.; Lee, M.; Lee, K.-K. Citrus Pests and Diseases Recognition Model Using Weakly Dense Connected Convolution Network. *Sensors* **2019**, *19*, 3195. [CrossRef]
19. Moskal, L.M.; Zheng, G. Retrieving Forest Inventory Variables with Terrestrial Laser Scanning (TLS) in Urban Heterogeneous Forest. *Remote Sens.* **2012**, *4*, 1–20. [CrossRef]
20. Schneider, F.D.; Leiterer, R.; Morsdorf, F.; Gastellu-Etchegorry, J.P.; Lauret, N.; Pfeifer, N.; Schaepman, M.E. Simulating imaging spectrometer data: 3D forest modeling based on LiDAR and in situ data. *Remote Sens. Environ.* **2014**, *152*, 235–250. [CrossRef]
21. Lian, X.; Dai, H.; Ge, L.; Cai, Y. Assessment of a house affected by ground movement using terrestrial laser scanning and numerical modeling. *Environ. Earth Sci.* **2020**, *79*, 2181–2185. [CrossRef]
22. Tong, X.; Liu, X.; Chen, P.; Liu, S.; Luan, K.; Li, L.; Liu, S.; Liu, X.; Xie, H.; Jin, Y.; et al. Integration of UAV-Based Photogrammetry and Terrestrial Laser Scanning for the Three-Dimensional Mapping and Monitoring of Open-Pit Mine Areas. *Remote Sens.* **2015**, *7*, 6635–6662. [CrossRef]
23. Yang, H.; Xu, X.; Xu, W.; Neumann, I. Terrestrial Laser Scanning-Based Deformation Analysis for Arch and Beam Structures. *IEEE Sens. J.* **2017**, *17*, 4605–4611. [CrossRef]
24. Xia, C.; Wang, L.; Chung, B.-K.; Lee, J.-M. In Situ 3D Segmentation of Individual Plant Leaves Using a RGB-D Camera for Agricultural Automation. *Sensors* **2015**, *15*, 20463–20479. [CrossRef] [PubMed]
25. Yun, T.; Jiang, K.; Li, G.; Eichhorn, M.P.; Fan, J.; Liu, F.; Chen, B.; An, F.; Cao, L. Individual tree crown segmentation from airborne LiDAR data using a novel Gaussian filter and energy function minimization-based approach. *Remote Sens. Environ.* **2021**, *256*, 112307. [CrossRef]

26. Polat, N.; Uysal, M. An investigation of tree extraction from UAV-based photogrammetric dense point cloud. *Arab. J. Geosci.* **2020**, *13*, 846–854. [CrossRef]
27. Ebrahimi, A.; Czarnuch, S. Automatic Super-Surface Removal in Complex 3D Indoor Environments Using Iterative Region-Based RANSAC. *Sensors* **2021**, *21*, 3724. [CrossRef]
28. Orozco-Del-Castillo, M.; Cárdenas-Soto, M.; Ortiz-Alemán, C.; Couder-Castañeda, C.; Urrutia-Fucugauchi, J.; Trujillo-Alcántara, A. A texture-based region growing algorithm for volume extraction in seismic data. *Geophys. Prospect.* **2017**, *65*, 97–105. [CrossRef]
29. Li, B.; Jiang, G.; Shao, W. Color correction based on point clouds alignment in the logarithmic RGB space. *Vis. Comput.* **2015**, *31*, 257–270. [CrossRef]
30. Xu, X.; Yang, H.; Neumann, I. A feature extraction method for deformation analysis of large-scale composite structures based on TLS measurement. *Compos. Struct.* **2018**, *184*, 591–596. [CrossRef]
31. Moreno, R.; Graña, M.; Madani, K.; Ramik, D. Image segmentation on spherical coordinate representation of RGB colour space. *IET Image Proc.* **2018**, *6*, 1275–1283. [CrossRef]
32. Zigh, E.; Kouninef, B.; Kadiri, M. Removing Shadows Using RGB Color Space in Pairs of Optical Satellite Images. *J. Indian Soc. Remote Sens.* **2017**, *45*, 431–441. [CrossRef]
33. Prema, C.E.; Vinsley, S.S.; Suresh, S. Multi Feature Analysis of Smoke in YUV Color Space for Early Forest Fire Detection. *Fire Technol.* **2016**, *52*, 1319–1342. [CrossRef]
34. Cho, W.; Jang, J.; Koschan, A.; Abidi, M.A.; Paik, J. Hyperspectral face recognition using improved inter-channel alignment based on qualitative prediction models. *Opt. Express.* **2016**, *24*, 27637–27662. [CrossRef]
35. Yılmaztürk, F. Full-automatic self-calibration of color digital cameras using color targets. *Opt. Express.* **2011**, *19*, 18164–18174. [CrossRef]
36. Czerniawski, T.; Sankaran, B.; Nahangi, M.; Haas, C.; Leite, F. 6D DBSCAN-based segmentation of building point clouds for planar object classification. *Autom. Constr.* **2018**, *88*, 44–58. [CrossRef]
37. Wu, G.; Zhu, Q.; Huang, M.; Guo, Y.; Qin, J. Automatic recognition of juicy peaches on trees based on 3D contour features and colour data. *Biosyst. Eng.* **2019**, *188*, 1–13. [CrossRef]
38. Tzortzis, G.; Likas, A. The MinMax k-Means clustering algorithm. *Pattern Recognit.* **2014**, *47*, 2505–2516. [CrossRef]
39. Ferraz, A.; Saatchi, S.; Mallet, C.; Meyer, V. Lidar detection of individual tree size in tropical forests. *Remote Sens. Environ.* **2016**, *183*, 318–333. [CrossRef]
40. Schmitt, M.; Shahzad, M.; Zhu, X.X. Reconstruction of individual trees from multi-aspect TomoSAR data. *Remote Sens. Environ.* **2015**, *165*, 175–185. [CrossRef]
41. Lang, F.; Yang, J.; Yan, S.; Qin, F. Superpixel Segmentation of Polarimetric Synthetic Aperture Radar (SAR) Images Based on Generalized Mean Shift. *Remote Sens.* **2018**, *10*, 1592. [CrossRef]
42. Gao, Y.; Yang, J.; Guo, L. Nonlocal oriented method for image denoising. *Opt. Eng.* **2011**, *50*, 030502. [CrossRef]
43. Ji, J.; Li, X.-Y. Unsupervised synthetic aperture radar image segmentation with superpixels in independent space based on independent component analysis. *J. Appl. Remote Sens.* **2014**, *8*, 083682. [CrossRef]
44. Tiegen, P.; Yinhua, W.; Tihua, W. Mean shift algorithm equipped with the intersection of confidence intervals rule for image segmentation. *Pattern Recognit. Lett.* **2007**, *28*, 268–277. [CrossRef]
45. Yu, W.; Tian, X.; Hou, Z.; Zha, Y.; Yang, Y. Multi-scale mean shift tracking. *IET Comput. Vision.* **2015**, *9*, 110–123. [CrossRef]
46. Kumar, P.; Dick, A. Adaptive earth movers distance-based Bayesian multi-target tracking. *IET Comput. Vision.* **2013**, *7*, 246–257. [CrossRef]
47. Ortiz-Coder, P.; Sánchez-Ríos, A. An Integrated Solution for 3D Heritage Modeling Based on Videogrammetry and V-SLAM Technology. *Remote Sens.* **2020**, *12*, 1529. [CrossRef]
48. Errington, A.F.C.; Daku, B.L.F. Temperature Compensation for Radiometric Correction of Terrestrial LiDAR Intensity Data. *Remote Sens.* **2017**, *9*, 356. [CrossRef]
49. Thomas, V.; Treitz, P.; McCaughey, J.H.; Morrison, I. Mapping stand-level forest biophysical variables for a mixedwood boreal forest using lidar: An examination of scanning density. *Can. J. For. Res.* **2006**, *36*, 34–47. [CrossRef]
50. Hopkinson, C.; Chasmer, L.; Young-Pow, C.; Treitz, P. Assessing forest metrics with a ground-based scanning lidar. *Can. J. For. Res.* **2004**, *34*, 573–583. [CrossRef]
51. Ning, X.; Li, F.; Tian, G.; Wang, Y. An efficient outlier removal method for scattered point cloud data. *PLoS ONE* **2018**, *13*, e0201280. [CrossRef] [PubMed]
52. Yan, L.; Liu, H.; Tan, J.; Li, Z.; Chen, C. A Multi-Constraint Combined Method for Ground Surface Point Filtering from Mobile LiDAR Point Clouds. *Remote Sens.* **2017**, *9*, 958. [CrossRef]
53. Le, Q.; Liscio, E. A comparative study between FARO Scene and FARO Zone 3D for area of origin analysis. *Forensic Sci. Int.* **2019**, *301*, 166–173. [CrossRef] [PubMed]
54. Dandois, J.P.; Baker, M.; Olano, M.; Parker, G.G.; Ellis, E.C. What is the Point? Evaluating the Structure, Color, and Semantic Traits of Computer Vision Point Clouds of Vegetation. *Remote Sens.* **2017**, *9*, 355. [CrossRef]
55. Lu, N.; Zhou, J.; Han, Z.; Li, D.; Cao, Q.; Yao, X.; Tian, Y.; Zhu, Y.; Cao, W.; Cheng, T. Improved estimation of aboveground biomass in wheat from RGB imagery and point cloud data acquired with a low-cost unmanned aerial vehicle system. *Plant Methods* **2019**, *15*, 1–16. [CrossRef]

56. Wen, S. Display gamut comparison with number of discernible colors. *J. Electron. Imaging* **2006**, *15*, 043001. [CrossRef]
57. Li, Q.; Cheng, X. Comparison of Different Feature Sets for TLS Point Cloud Classification. *Sensors* **2018**, *18*, 4206. [CrossRef]
58. Duong, T.; Beck, G.; Azzag, H.; Lebbah, M. Nearest neighbour estimators of density derivatives, with application to mean shift clustering. *Pattern Recognit. Lett.* **2016**, *80*, 224–230. [CrossRef]
59. Öztekin, I.; Long, N.M.; Badre, D. Optimizing Design Efficiency of Free Recall Events for fMRI. *J. Cognit. Neurosci.* **2010**, *22*, 2238–2250. [CrossRef]
60. Ray, W.D. Multiple Regression and Analysis of Variance. *J. Oper. Res. Soc.* **2017**, *28*, 611–612. [CrossRef]
61. Xu, J.-X.; Ma, J.; Tang, Y.-N.; Wu, W.-X.; Shao, J.-H.; Wu, W.-B.; Wei, S.-Y.; Liu, Y.-F.; Wang, Y.-C.; Guo, H.-Q. Estimation of Sugarcane Yield Using a Machine Learning Approach Based on UAV-LiDAR Data. *Remote Sens.* **2020**, *12*, 2823. [CrossRef]
62. LJarron, L.R.; Coops, N.C.; MacKenzie, W.H.; Tompalski, P.; Dykstra, P. Detection of sub-canopy forest structure using airborne LiDAR. *Remote Sens. Environ.* **2020**, *244*, 111770–111782. [CrossRef]
63. Arnó, J.; Escolà, A.; Masip, J.; Rosell-Polo, J.R. Influence of the scanned side of the row in terrestrial laser sensor applications in vineyards: Practical consequences. *Precis. Agric.* **2015**, *16*, 119–128. [CrossRef]
64. Renard, F.; Voisin, C.; Marsan, D.; Schmittbuhl, J. High resolution 3D laser scanner measurements of a strike-slip fault quantify its morphological anisotropy at all scales. *Geophys. Res. Lett.* **2006**, *33*, 4305-1–4305-4. [CrossRef]
65. Jackson, S.S.; Bishop, M.J.; Leese, D.L.; Lord, E.M. High-resolution 3D laser imaging of various surfaces in minefields and implications for surface modeling. *Proc. SPIE Int. Soc. Opt. Eng.* **2005**, *5794*, 857–865. [CrossRef]
66. Hämmerle, M.; Höfle, B. Effects of Reduced Terrestrial LiDAR Point Density on High-Resolution Grain Crop Surface Models in Precision Agriculture. *Sensors* **2014**, *14*, 24212–24230. [CrossRef]
67. Khazaei, J.; Naghavi, M.; Jahansouz, M.; Salimi-Khorshidi, G. Yield Estimation and Clustering of Chickpea Genotypes Using Soft Computing Techniques. *Agron. J.* **2008**, *100*, 1077–1087. [CrossRef]
68. Genta, G.; Minetola, P.; Barbato, G. Calibration procedure for a laser triangulation scanner with uncertainty evaluation. *Opt. Lasers Eng.* **2016**, *86*, 11–19. [CrossRef]
69. Wang, L.; Muralikrishnan, B.; Rachakonda, P.; Sawyer, D. Determining geometric error model parameters of a terrestrial laser scanner through two-face, length-consistency, and network methods. *Meas. Sci. Technol.* **2017**, *28*, 065016. [CrossRef]
70. Liu, S.; Xu, D.; Li, Y.-F.; Shen, F.; Zhang, D.-P. Nanoliter Fluid Dispensing Based on Microscopic Vision and Laser Range Sensor. *IEEE Trans. Ind. Electron.* **2017**, *64*, 1292–1302. [CrossRef]
71. Srinivasan, S.; Popescu, S.; Eriksson, M.; Sheridan, R.; Ku, N.-W.J.R.S. Terrestrial Laser Scanning as an Effective Tool to Retrieve Tree Level Height, Crown Width, and Stem Diameter. *Remote Sens.* **2015**, *7*, 1877–1896. [CrossRef]
72. Zhang, Y.; Migliavacca, M.; Penuelas, J.; Ju, W. Advances in hyperspectral remote sensing of vegetation traits and functions. *Remote Sens. Environ.* **2020**, *252*, 112121–112126. [CrossRef]
73. Axelsson, P. Processing of laser scanner data—Algorithms and applications. *ISPRS J. Photogramm. Remote Sens.* **1999**, *54*, 138–147. [CrossRef]
74. Koetz, B.; Sun, G.; Morsdorf, F.; Ranson, K.J.; Kneubühler, M.; Itten, K.; Allgöwer, B. Fusion of imaging spectrometer and LIDAR data over combined radiative transfer models for forest canopy characterization. *Remote Sens. Environ.* **2007**, *106*, 449–459. [CrossRef]
75. Ghamkhar, K.; Irie, K.; Hagedorn, M.; Hsiao, J.; Fourie, J.; Gebbie, S.; Hoyos-Villegas, V.; George, R.; Stewart, A.; Inch, C.; et al. Real-time, non-destructive and in-field foliage yield and growth rate measurement in perennial ryegrass (*Lolium perenne* L.). *Plant Methods* **2019**, *15*, 72. [CrossRef] [PubMed]
76. Guan, H.; Yu, Y.; Ji, Z.; Li, J.; Zhang, Q. Deep learning-based tree classification using mobile LiDAR data. *Remote Sens. Lett.* **2015**, *6*, 864–873. [CrossRef]
77. Chen, J.; Chen, Y.; Liu, Z. Classification of Typical Tree Species in Laser Point Cloud Based on Deep Learning. *Remote Sens.* **2021**, *13*, 4750. [CrossRef]
78. Rehush, N.; Abegg, M.; Waser, L.T.; Brändli, U.-B. Identifying Tree-Related Microhabitats in TLS Point Clouds Using Machine Learning. *Remote Sens.* **2018**, *10*, 1735. [CrossRef]
79. Xi, Z.; Hopkinson, C.; Chasmer, L. Filtering Stems and Branches from Terrestrial Laser Scanning Point Clouds Using Deep 3-D Fully Convolutional Networks. *Remote Sens.* **2018**, *10*, 1215. [CrossRef]